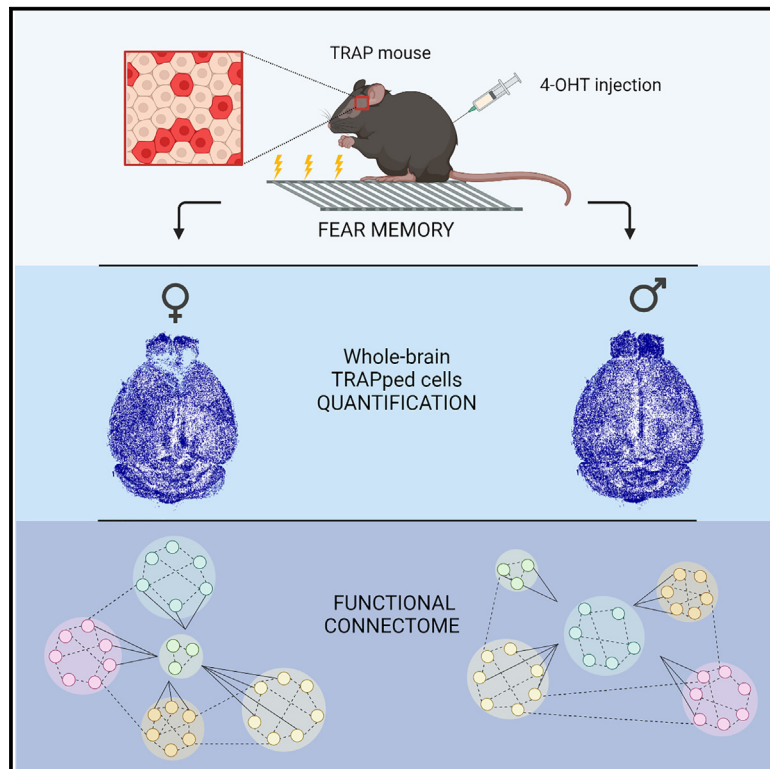# Brain-wide neuron quantification toolkit reveals strong sexual dimorphism in the evolution of fear memory

Graphical abstract

Authors

Alessandra Franceschini,
Giacomo Mazzamuto,
Curzio Checcucci, ...,
Bianca Ambrogina Silva,
Francesco Saverio Pavone,
Ludovico Silvestri

Correspondence

franceschini@lens.unifi.it (A.F.),
silvestri@lens.unifi.it (L.S.)

In brief

Franceschini et al. develop BRANT, a whole-brain pipeline that combines tissue clearing, high-resolution light-sheet microscopy, and automated 3D image analysis in order to reveal neural circuits mediating memory encoding, consolidation, and retrieval. Exploiting BRANT, the authors find a strong sexual dimorphism in the evolution of fear memory.

Highlights

- BRANT enables scalable, high-resolution analysis of neuronal patterns

- BRANT reveals strong sexual dimorphism during memory formation, consolidation, and retrieval

- The brain regions identified as hubs for fear memory evolve over time

CellPress

Cell Reports

Resource

Brain-wide neuron quantification toolkit reveals strong sexual dimorphism in the evolution of fear memory

Alessandra Franceschini,[1,2,*] Giacomo Mazzamuto,[1,2,3] Curzio Checcucci,[4] Lorenzo Chicchi,[2] Duccio Fanelli,[2] Irene Costantini,[1,5] Maria Beatrice Passani,[6] Bianca Ambrogina Silva,[7,8] Francesco Saverio Pavone,[1,2,3] and Ludovico Silvestri[1,2,3,9,*]
[1]European Laboratory for Non-linear Spectroscopy (LENS), University of Florence, Sesto Fiorentino, Italy
[2]Department of Physics and Astronomy, University of Florence, Sesto Fiorentino, Italy
[3]National Institute of Optics - National Research Council (CNR-INO), Sesto Fiorentino, Italy
[4]Department of Information Engineering (DINFO), University of Florence, Florence, Italy
[5]Department of Biology, University of Florence, Florence, Italy
[6]Department of Health Sciences, University of Florence, Florence, Italy
[7]National Research Council of Italy, Institute of Neuroscience, Milan, Italy
[8]IRCCS Humanitas Research Hospital, Lab of Circuits Neuroscience, Rozzano, Milan, Italy
[9]Lead contact
*Correspondence: franceschini@lens.unifi.it (A.F.), silvestri@lens.unifi.it (L.S.)
https://doi.org/10.1016/j.celrep.2023.112908

SUMMARY

Fear responses are functionally adaptive behaviors that are strengthened as memories. Indeed, detailed knowledge of the neural circuitry modulating fear memory could be the turning point for the comprehension of this emotion and its pathological states. A comprehensive understanding of the circuits mediating memory encoding, consolidation, and retrieval presents the fundamental technological challenge of analyzing activity in the entire brain with single-neuron resolution. In this context, we develop the brain-wide neuron quantification toolkit (BRANT) for mapping whole-brain neuronal activation at micron-scale resolution, combining tissue clearing, high-resolution light-sheet microscopy, and automated image analysis. The robustness and scalability of this method allow us to quantify the evolution of activity patterns across multiple phases of memory in mice. This approach highlights a strong sexual dimorphism in recruited circuits, which has no counterpart in the behavior. The methodology presented here paves the way for a comprehensive characterization of the evolution of fear memory.

INTRODUCTION

Fear responses are functionally adaptive behaviors that can be induced by a direct encounter with a threat or with situations previously associated with a threat. Indeed, given its high survival value, the capability to remember potential threats is highly conserved across species.[1] Although "fear" refers to a human emotion, with a specific connotation in our minds not directly accessible in other animals, we can nevertheless study defensive responses induced by aversive events in animal models using standard behavioral paradigms like contextual fear conditioning (CFC) and inhibitory avoidance (IA).[2] Fear induces many changes at different levels, from molecular and cellular to circuit ones.[3,4] These permanent changes represent the physical trace of memory, commonly referred to as "engram." In the last years, neuroscientists have made many steps forward in the knowledge of the molecular and cellular mechanisms underlying memory formation, consolidation, and retrieval.[4–7] Furthermore, several brain areas, most prominently the hippocampus, the

amygdala, and the prefrontal cortex, have been identified as important centers for memory processing.[2] However, several studies highlighted the involvement of many other regions,[8–10] supporting the hypothesis that memory is distributed and dispersed across the entire brain; from this perspective, the study of a single or a few brain areas limits the comprehension of mechanisms underlying fear memory. The study of limited brain regions leads to a fragmented view that makes the global vision rarely interpretable; therefore, many significant questions about fear mechanisms and dynamics have yet to be explained.

The paucity of studies addressing fear memory substrates at the brain-wide level is mainly due to the technical limitations in large-scale analysis of neuronal activity. From a methodological point of view, understanding how neuronal networks drive this type of memory requires techniques for whole-brain activation mapping. In this respect, a promising strategy is to tag activated neurons *in vivo* through immediately early gene (IEG) approaches and image them subsequently *ex vivo* by 3D optical tools such as light-sheet microscopy (LSM). The coupling of clearing
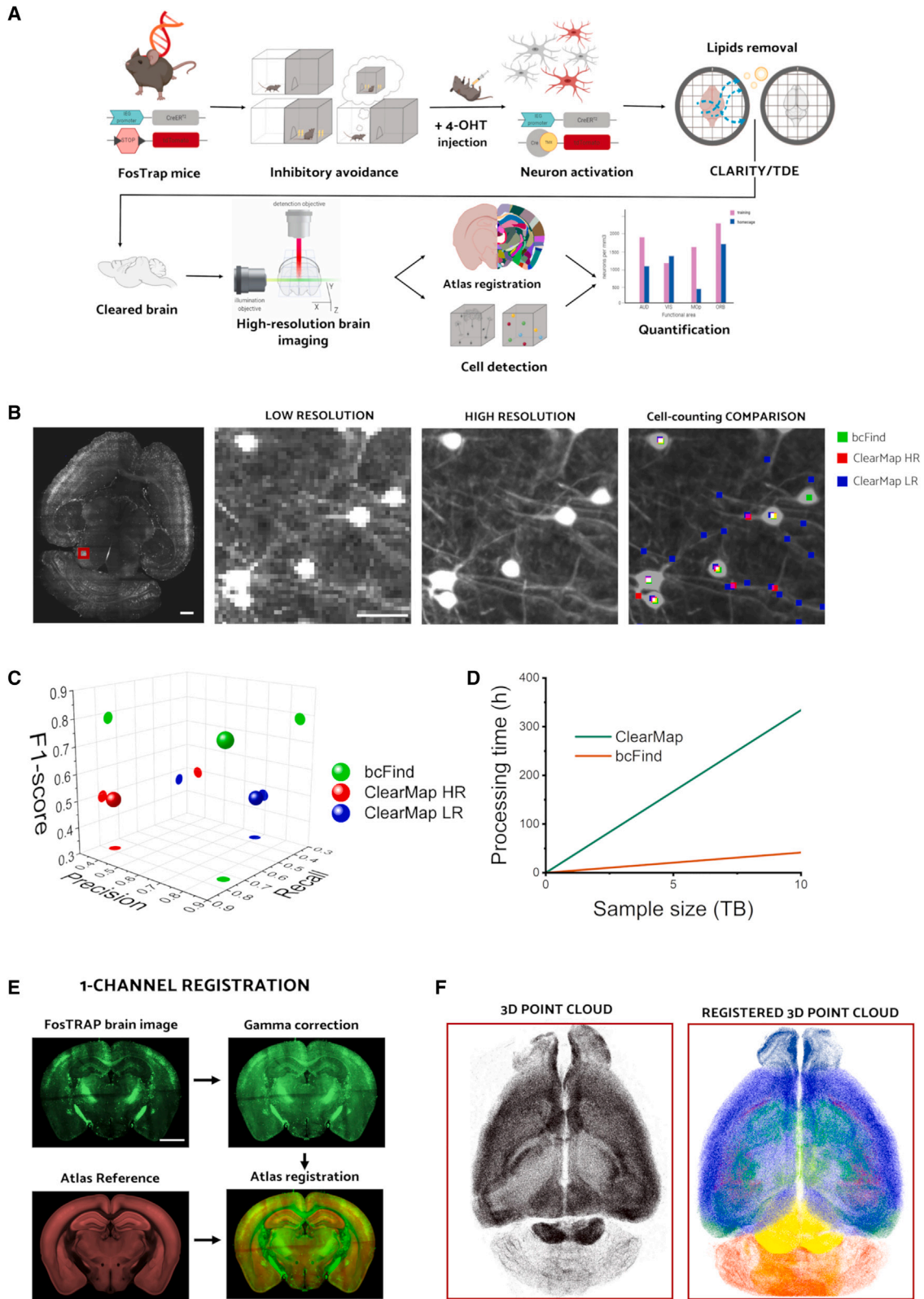
techniques, like CLARITY,[11] iDISCO,[12] or CUBIC,[13] with LSM has enabled the brain-wide mapping of cFos+ neurons activated in different behavioral contexts.[13,14,15] However, IEG transgenic tools[16–19] label the entire neuronal cell, including axons and dendrites, making image analysis more challenging as compared to anti-cFos immunostaining, which is confined to the nucleus.[19] In this respect, subcellular resolution is needed to disentangle the contribution from neuronal processes and somata. Since the data size scales with the third power of the sample linear dimensions, even a moderate increase in spatial resolution (e.g., 2×) leads to a large increase of in the amount of data to be processed (8× in our example). Unfortunately, available analysis tools[14] are not capable of routinely handling TB-sized datasets, limiting brain-wide activation analysis to anti-cFos immunostaining. On the other hand, the ability to quantify cells labeled through IEG-based transgenic strategies would enable further investigation on the same animal after tagging of activated neurons.[17,15]

From a clinical point of view, the study of fear memory requires scalable methods to analyze large cohorts of subjects. This is necessary to clarify how different neuronal circuits are disrupted in disease states such as in post-traumatic stress disorder (PTSD). Indeed, understanding how memory works and changes over time would imply analysis of multiple time points and of diverse experimental classes.

The lifetime prevalence of PTSD is about 10%–12% in women and 5%–6% in men.[20] Women have a two/three times higher risk of developing PTSD compared with men.[21] In spite of this striking difference in prevalence and risk between male and female subjects, sex difference studies are only partially considered in the field of neuroscience since researchers typically favor male mice rather than female mice in their studies, with a ratio of 5.5 to 1.[22] This disproportion does not consider the sex statistical differences in the lifetime of many pathologies, suggesting serious implications for healthcare in women. The factors that influence the different lifetimes in PTSD vary from biological to psychological ones.[21] Also, in the context of whole-brain mapping, the few studies published hitherto focused only on the male population.[15,23–26]

Here, we present BRANT (brain-wide neuron quantification toolkit), a new pipeline for whole-brain mapping, exploiting TRAP mice,[16] high-resolution LSM, and terabyte-scale image processing. Using BRANT, we analyze the evolution of whole-brain neural circuits recruited upon aversive memory in females

and males. We find strong sexual dimorphism in the evolution of whole-brain networks underlying fear memory, both at the levels of activation patterns and of functional connectivity.

RESULTS

BRANT enables scalable, high-resolution analysis of neuronal activity patterns in behaviorally relevant cohorts

Any method aiming at complementing behavioral analysis with physiological or anatomical data must be applicable to dozens of samples, allowing its use in a statistically significant number of animals for each behavioral group. With this important constraint in mind, we developed BRANT, a scalable and user-friendly pipeline for 3D analysis of whole-brain activation patterns that combines FosTRAP transgenic strategy,[16] CLARITY/TDE,[27] high-resolution RAPID-enabled LSM,[28] and 3D automated data analysis[29] (Figure 1A). BRANT was validated using a classical paradigm, i.e., step-through passive IA. After the behavioral task, mice are injected with 4-hydroxytamoxifen (4-OHT) to drive Cre-mediated recombination in cFos-expressing neurons.[16]

Importantly, since the reporter fluorescent protein (tdTomato) is not confined to the soma but is expressed in the entire neuron, high-resolution imaging is required to disentangle dense environments (Figure 1B). To this aim, 3D whole-brain reconstructions were achieved by optimizing clearing and imaging protocols. All brains were made optically transparent using a modified CLARITY/TDE protocol allowing moderate expansion of tissue (27% linearly).[30] This isotropic change in sample size offered the possibility to discriminate single cells in densely labeled structures. Samples were then imaged using a custom-made LSM with confocal line detection, able to reconstruct mesoscopic samples with microscale resolution.[31] Through a system for real-time stabilization of light-sheet alignment, called RAPID, we were able to maintain high resolution across the entire sample volume[28] (Video S1). Since RAPID operates simultaneously with image detection, no acquisition overhead is introduced.

Each brain reconstruction comprises about 16 terabytes of raw data with a voxel size of $0.65 \times 0.65 \times 2 \ \mu m^3$. This data size is incompatible with a cohort study, as it would require storage capabilities in the order of 1 petabyte for a single study. For

Figure 1. Experimental pipeline

(A) Schematic representation of various steps constituting the experimental pipeline. FosTRAP mice underwent the step-through IA task. Injection of 4-OHT drives permanent expression of tdTomato in activated neurons. After perfusion, all brains were processed with CLARITY/TDE and imaged with a high-resolution RAPID-enabled LSM. High-resolution imaging was fundamental for cell detection and 3D automated analysis. All brains were registered to the Allen Brain Atlas. tdTomato+ neurons are automatically detected and quantified across all behavioral groups.
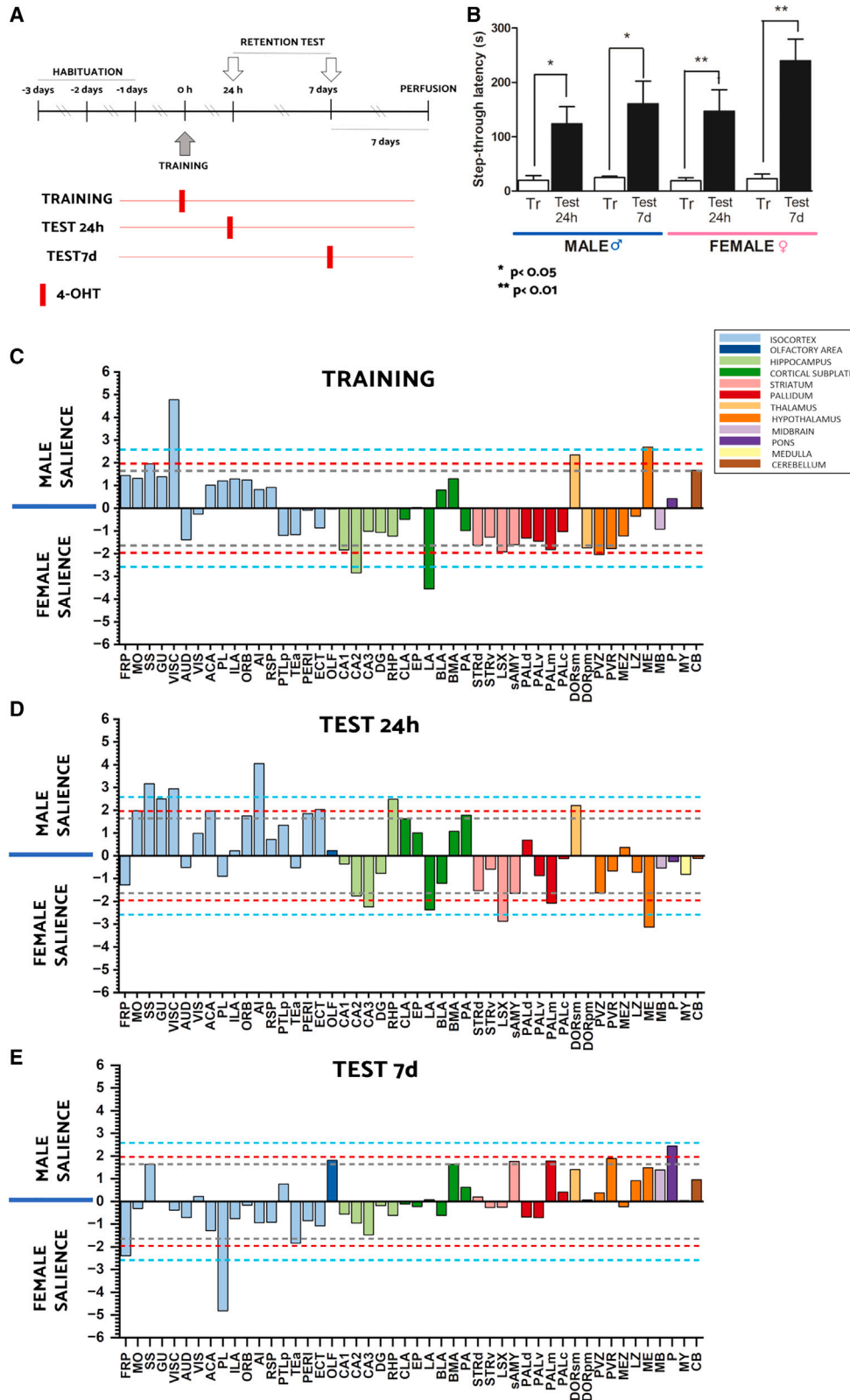
(B) Virtual slice extracted from a whole-brain tomography; scale bar, 1,000 μm (left). The red square identifies a small region zoomed in on the other subpanels; scale bar, 50 μm. Low- and high-resolution zoom ins, corresponding to voxel sizes of $4 \times 4 \times 4$ and $0.65 \times 0.65 \times 2 \ \mu m^3$, respectively (center). Results of cell counting in this subvolume obtained with bcFind and ClearMap (right).

(C) Comparison of the localization performance (precision, recall, and F-1 score) of bcFind and ClearMap at low resolution (ClearMap LR) and high resolution (ClearMap HR).

(D) Data throughput of bcFind and ClearMap in 3D automated analysis.

(E) One channel image registration to the Atlas. Gamma correction is applied to the FosTRAP image; scale bar, 300 μm. Image with high contrast is used for the Atlas registration.

(F) The point cloud obtained with bcFind (left) is finally warped to the reference atlas (right). In the right image, points are colored according to the brain region to which they belong.

A

HABITUATION

-3 days   -2 days   -1 days   0 h   24 h   7 days   PERFUSION

RETENTION TEST

7 days

TRAINING

TRAINING

TEST 24h

TEST7d

| 4-OHT

B

Step-through latency (s)

Tr | Test 24h | Tr | Test 7d | Tr | Test 24h | Tr | Test 7d

MALE ♂   FEMALE ♀

* p< 0.05
** p< 0.01

C

TRAINING

MALE SALIENCE / FEMALE SALIENCE

ISOCORTEX
OLFACTORY AREA
HIPPOCAMPUS
CORTICAL SUBPLATE
STRIATUM
PALLIDUM
THALAMUS
HYPOTHALAMUS
MIDBRAIN
PONS
MEDULLA
CEREBELLUM

FRP MO SS GU VISC AUD VIS ACA PL ILA ORB AI RSP PTLp TEa PERI ECT OLF CA1 CA2 CA3 DG RHP CLA EP LA BLA BMA PA STRd STRv LSX sAMY PALd PALv PALm PALc DORsm DORpm PVZ PVR MEZ LZ ME MB P MY CB

D

TEST 24h

MALE SALIENCE / FEMALE SALIENCE

FRP MO SS GU VISC AUD VIS ACA PL ILA ORB AI RSP PTLp TEa PERI ECT OLF CA1 CA2 CA3 DG RHP CLA EP LA BLA BMA PA STRd STRv LSX sAMY PALd PALv PALm PALc DORsm DORpm PVZ PVR MEZ LZ ME MB P MY CB

E

TEST 7d

MALE SALIENCE / FEMALE SALIENCE

FRP MO SS GU VISC AUD VIS ACA PL ILA ORB AI RSP PTLp TEa PERI ECT OLF CA1 CA2 CA3 DG RHP CLA EP LA BLA BMA PA STRd STRv LSX sAMY PALd PALv PALm PALc DORsm DORpm PVZ PVR MEZ LZ ME MB P MY CB

(legend on next page)

this reason, the acquired datasets were first compressed by a factor of 20 using the 16-bit lossy JPEG-2000 format, thus reducing disk usage while still retaining overall good image quality and detail level. Images were then stitched using ZetaStitcher (https://lens-biophotonics.github.io/ZetaStitcher/), a custom-made Python software for large volumetric stitching specifically developed for LSM. An important feature of ZetaStitcher is VirtualFusedVolume, an application programming interface (API) that provides seamless and effective access to high-resolution data by simply providing the spatial coordinates of the subvolume of interest within the virtually fused volume. In this way, large volumes can be programmatically processed in smaller chunks in a distributed environment and without user intervention, a key requirement to process the large datasets produced by high-resolution LSM. Fluorescently labeled activated neurons were detected using BrainCell Finder (bcFind).[29] This 3D automated analysis relies on a deep-learning approach, based on a U-Net architecture, widely used in the image analysis field,[32] to recognize specific structures in complex datasets. Indeed, since tdTomato is expressed also in neuronal processes, the application of standard methods based on thresholds and blob detectors is not feasible (Figure 1B). The task of our U-Net is to transform raw images, containing many disturbing objects (like axons, dendrites, and vessels), into ideal images that include only small spheres at the location of neuronal bodies. In the images transformed by the U-Net, a basic blob detector algorithm can then effectively localize the fluorescent cell bodies. The performance of this method was evaluated on 3,383 manually labeled cells, measuring the number of true positives (TP, cells detected both by the human annotator and the algorithm), false positives (FP, cells detected by the algorithm alone), and false negatives (FN, cells detected by the human annotator but missed by the algorithm). We obtained precision = TP/(TP + FP) equal to 0.84, recall = TP/(TP + FN) 0.74, and F1 score = 0.78. F1 is defined as the harmonic mean of precision and recall, $1/F1 = (1/P + 1/R)/2$. We compared the accuracy of bcFind with that obtained using ClearMap, a widely used software for cFos$^+$ cell detection in cleared brains.[14] To simulate the typical application settings of the method, we tested it also on images downscaled to a standard voxel size of $4 \times 4 \times 4 \ \mu m^3$ (Figure 1C). ClearMap analysis showed poor performance both with high- (precision: 0.36, recall: 0.78, F1: 0.49) and low-resolution data (precision: 0.69, recall: 0.35, F1: 0.46). This is not surprising since the method has been developed to detect spherical-like objects (like cFos-stained nuclei) and not complex neuronal cells. Parameters used for BRANT U-Net and for ClearMap are reported in Tables S1 and S2, respectively.

Given that raw data amount to about 16 terabytes per brain, another fundamental feature is computational scalability. bcFind can be operated in batch mode on a computing cluster, enabling image processing at a rate that is ultimately limited only by computational power. In our case, using a cluster with 8 GPUs (NVIDIA GeForce RTX 2080Ti), we were able to process data at about 240 GB/h, about 1 order of magnitude faster than the reported speed of ClearMap[14] (Figure 1D). Importantly, this is not a comparison about the absolute speed of both algorithms—i.e., these data do not mean that bcFind is faster than ClearMap when using the same resources—but rather is a comparison about the capabilities of the two software to effectively run on large-scale parallelized environments—meaning that in practical settings, bcFind is faster when used on terabyte (TB)-sized datasets.

To compare cell counts across multiple subjects, 3D brain datasets are spatially aligned to the Allen Brain Reference Atlas using Advanced Normalization Tools (ANTs).[33] Different from previous reports, we did not acquire a secondary channel for atlas registration but rather applied a strong gamma correction to reduce the contrast between tissue autofluorescence and the signal from fluorescent protein (Figures 1E and 1F). We found a registration accuracy of about 300 μm (see STAR Methods), which is comparable to that obtained by ClearMap.[14] Notably, the approach implemented here reduces the cost and complexity of the microscope used since only one camera is needed in the microscope and the size of acquired datasets is not duplicated. Of note, all brain areas were included and grouped for this study, manually selecting 48 non-overlapping macro areas. We decided to use larger areas (the Allen Reference Atlas has more than 1,000 subregions) based on the measured registration accuracy to avoid misassignment of cells.

In conclusion, the combination of fast high-resolution imaging and scalable 3D analysis for processing subcellular information is the core of this pipeline, enabling quantification of active neuronal ensembles in behaviorally relevant cohorts (Videos S2 and S3).

BRANT analysis reveals sexually dimorphic patterns of brain activation in different phases of aversive memory

BRANT was applied to study the time evolution of neuronal activity over the course of fear memory (Figure 2A). In order to answer our biological question, we used step-through IA as a behavioral paradigm in which mice learn to associate a particular context (i.e., white/black box) with an aversive event (i.e., a mild foot shock). Differently from the standard CFC, IA implies decision-making since mice can decide whether to step into the dark

Figure 2. Behavioral task and neuronal activity analysis
(A) Schematic representation of the experimental paradigm. Animals are handled for 3 days before training. During the training session, all mice receive a foot shock (0.3 mA, shock duration 2 s, delay after closing door 0.5 s). Memory retention test is performed 24 h or 7 days after training. By the 4-OHT injection at three time points, mice were divided in three experimental classes: training, test 24 h, or test 7 days.
(B) The comparisons of acquisition and retention latency times are analyzed by two-way ANOVA, followed by Bonferroni's post hoc comparisons tests (*p < 0.05, **p < 0.01, training n = 6 males and n = 4 females, test 24 h n = 5 males and n = 6 females, and test 7 days n = 4 males and n = 4 females). Data are expressed as means ± SEM of 4–6 animals for each group.
(C–E) PLS analysis of cFos expression between the two sexes in all experimental classes: training (C), test 24 h (D), and test 7 days (E). Salience scores, normalized by standard deviation calculated with bootstrap (right), identify regions that maximally differentiate between these conditions. The gray, red, and blue lines reflect, respectively, salience scores of 1.64 (p < 0.1), 1.96 (p < 0.05), and 2.58 (p < 0.01).

Table 1. List of brain regions

Abbreviation	Long name	Brain region
FRP	frontal pole	isocortex
MO	somatomotor areas	isocortex
SS	somatosensory areas	isocortex
GU	gustatory areas	isocortex
VISC	visceral areas	isocortex
AUD	auditory areas	isocortex
VIS	visual area	isocortex
ACA	anterior cingulate area	isocortex
PL	prelimbic area	isocortex
ILA	infralimbic area	isocortex
ORB	orbital area	isocortex
AI	agranular insular area	isocortex
RSP	retrosplenial area	isocortex
PTLp	posterior parietal association areas	isocortex
Tea	temporal association areas	isocortex
PERI	perirhinal area	isocortex
ECT	ectorhinal area	isocortex
OLF	olfactory areas	olfactory areas
DG	dentate gyrus	hippocampal formation
CA1	field CA1	hippocampal formation
CA2	field CA2	hippocampal formation
CA3	field CA3	hippocampal formation
RHP	retrohippocampal region	hippocampal formation
CLA	claustrum	cortical subplate
EP	endopiriform nucleus	cortical subplate
LA	lateral amygdalar nucleus	cortical subplate
BLA	basolateral amygdalar nucleus	cortical subplate
BMA	basomedial amygdalar nucleus	cortical subplate
PA	posterior amygdalar nucleus	cortical subplate
STRd	striatum dorsal region	striatum
STRv	striatum ventral region	striatum
LSX	lateral septal complex	striatum
sAMY	striatum-like amygdalar nuclei	striatum
PALd	dorsal pallidum	pallidum
PALv	ventral pallidum	pallidum
PALm	medial pallidum	pallidum
PALc	caudal pallidum	pallidum
DORsm	thalamus, sensory motor	thalamus
DORpm	thalamus, polymodal association	thalamus
PVZ	periventricular zone	hypothalamus
PVR	periventricular region	hypothalamus
MEZ	hypothalamic medial zone	hypothalamus
LZ	hypothalamic lateral zone	hypothalamus

Table 1. *Continued*

Abbreviation	Long name	Brain region
ME	median eminence	hypothalamus
MB	midbrain	midbrain
P	pons	pons
MY	medulla	medulla
CB	cerebellum	cerebellum

The list of brain regions used for activation analysis.

compartment when they are subsequently tested for memory retention.[2] Indeed, the latency time to enter the dark compartment is used as a direct measurement of memory. This task relies on a single training session and produces robust memory that is easily quantifiable and long lasting. By using IA, we selected three experimental groups based on three different memory phases describing the evolution of fear memory, from encoding to retrieval: a training group was selected to study fear encoding, while test groups at 24 h and 7 days after training were selected to explore the recent and long-term fear memory retrieval, respectively (Figure 2A). As expected, latency times of training groups (in which the latency to enter the shock compartment is measured in the habituation period) were significantly different compared with the latency times of the respective test groups. Statistical analyses indicate that latency times were influenced only by the experimental class and not by sex (two-way ANOVA, followed by Bonferroni's post hoc comparisons tests) (Figure 2B). Indeed, there was no significant difference in training performances in any group examined or between various test groups (Figure 2B). This indicates that all mice, independently from their sex, formed a memory of the training experience even though the shock intensity (0.3 mA) was weaker than that classically used.[34,35] The value of shock intensity was selected within a range in which the behavioral outcome at retrieval shows distinct inter-subject variability, with the aim to point out the contribution of neuronal activation resulting from the decision-making process. (Figure S1). Although the results from IA did not highlight any differences between male and female groups, the quantification of activated neurons (cFos) in 48 brain regions (for a complete listing of brain regions, see Table 1) revealed a strong sexual dimorphism in the underlying neuronal activity pattern. To obtain a statistically robust comparison of the activation patterns between male and female subjects, we performed mean-centered partial least squares (PLS) analysis.[36] This method identifies a set of latent variables ("contrasts") in the space formed by the different experimental conditions and a corresponding set of "saliences," i.e., the contribution of different brain areas in differentiating the samples between the different contrasts. Notably, differently from pairwise comparison of cell counts between different experimental classes, this method does not require correction for multiple sample comparisons, resulting in overall higher statistical power.[36]

The vectors of PLS contrasts that discriminate between sexes have different structures at different time points (training and test 24 h and test 7 days after training), revealing distinct patterns of cFos expression between males and females in our experimental groups (Figures 2C–2E).
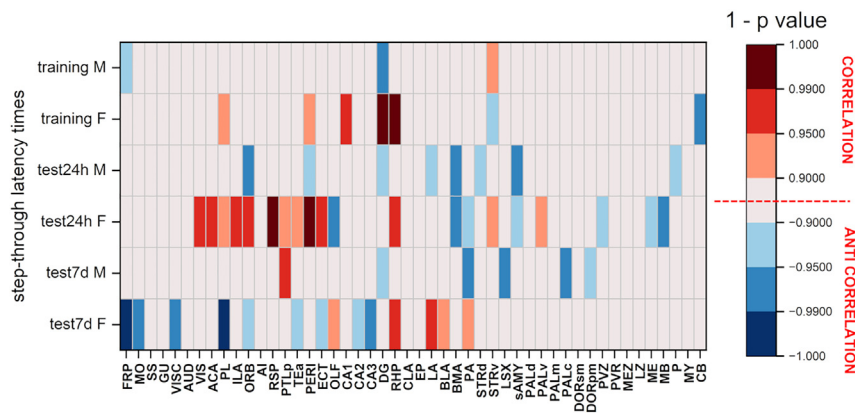
Figure 3. Pairwise correlation of latency time with neuronal activity in each brain area
Pearson correlation heatmaps. Here, heatmaps represent the correlation between the number of tdTomato+ neurons in each region and the latency time mice spend to step through into the dark compartment. On the right side of the plot, different colors correspond to different significant degrees ($1 - p$ values).

Using this unbiased analysis, a strong sexual dimorphism in the recruitment of several brain areas in each memory phase was observed. This dimorphism emerges not only in regions classically considered to be involved in aversive memory such as the prefrontal cortex, the amygdala, and the hippocampus but also in brain areas less known for their contribution in this function such as the pallidum, the striatum, the thalamus, and other subcortical regions. The differences of cFos expression (Figures 2C–2E) in all brain regions seem to fade over time, from the training group to the test 7 days group. Indeed, 7 days after training, there is an alignment of cFos patterns between sexes with only 3 brain areas (frontal pole [FRP], prelimbic area [PL], pons [P]) being significantly different with p <0.05 (Figure 2E). At training and test 24 h after training, male mice showed an increased cFos expression in the cerebral cortex (somatosensory area [SS], gustatory area [GU], visceral area [VISC], agranular insular area [AI], ectorhinal area [ECT]), while female mice showed this in subcortical regions, with the exception of the thalamus, which is always more activated in the male group at all time points (Figures 2C and 2D). Notably, hippocampal regions showed a general trend of increased activity in females as compared with males at all time points, although these differences were less evident at 7 days. In particular, the CA2 showed significantly higher activation in females compared with males at both training and 24 h test, while the CA1 displayed a marked increase at training and the CA3 at test 24 h. At 7 days after training, male mice are associated with an increased cFos expression in the P and other evolutionary older brain regions, while female mice are associated with increased cFos expression in the associative cortex (FRP and PL) (Figure 2E). An interesting case is represented by the median eminence that is more activated at training in males but at test 24 h in females (Figures 2C and 2D).

These data indicate that males and females activate, on average, different neuronal patterns in distinct phases of aversive memory, highlighting a strong sexual dimorphism that is, notably, not reflected in behavioral differences.

Neuronal activity correlates with behavioral outcome in different brain regions in females and males

BRANT application showed how activity patterns involved in fear memory differ in male and female mice. The results obtained by

PLS, based on tdTomato+ neuron quantifications in each brain region, showed the areas that account more for the difference in activity between experimental groups, each one corresponding to a specific memory phase. Thus, this analysis highlights variations between different experimental classes at the population level but is not appropriate to investigate the inter-subject variability inside the same experimental group. Indeed, latency times were significantly dispersed, underlining variable behavioral responses between different mice (Figures 2A and S1). To investigate whether neuronal activation of specific areas can be accounted for the behavioral variability observed, we performed a cross-correlation analysis between regional counts and latency times (Figure 3). This analysis led to the identification of strong correlations or anti-correlations (p < 0.01) for different areas in different experimental classes. Importantly, brain regions that correlate with behavior are different for both sexes, underlining a sexual dimorphism also in this type of analysis (Figure 3). As expected, the amygdala, the hippocampus, and the prefrontal cortex are correlated with the step-through latency times, but also, the activation of areas such as the pallidum, the striatum, the pons, and other regions less known to be involved in fear memory correlates with the time mice spent in the bright cage before stepping through into the dark compartment.

For male and female training groups, latency times are not directly related to fear but instead to the exploration of the environment. For this reason, in line with the literature, the brain areas more correlated with these latency times are the CA1, the dentate gyrus (DG), and the retrohippocampal region (RHP), relevant for specific contextual information[2,37,38]; the striatum ventral region (STRv), which supports the rapid discrimination of uncertain threats that is necessary for the first contextual exploration[39]; the PL, which regulates fear expression[40]; the PERI, which encodes the delay between conditioned and unconditioned stimuli[41]; and the cerebellum (CB), which participates in movement and is an important autonomic control center as part of an integrated network regulating fear.[42] Notably, the CB is anti-correlated with training latency times, suggesting that its activation leads to reduced explorative behavior. Here, male subjects show a significant correlation between behavior and neuronal activation only in the STRv, a region anti-correlated with latency times in female mice. On the other hand, in female subjects, strong correlation is observed in the CA1, the DG, the RHP, the PL, and the PERI, while a clear anti-correlation is found in the CB.

Latency times during test sessions are usually considered in IA as a measure of fear memory retention.[2] 24 h after training, a

striking sexual dimorphism is observed in the orbital area (ORB) and the perirhinal area (PERI), where higher activation correlates with longer and shorter latency times in females and males, respectively. In general, we observe that, in female mice, associative cortical areas are more activated when animals wait longer before crossing to the dark compartment. These data are in line with previous literature highlighting the crucial role played by the associative cortex in the formation of fear memory.[43,44] Sexual dimorphism tends to be less pronounced in deeper brain areas, like the basomedial amygdalar nucleus (BMA) and the striatum-like amygdalar nucleus (sAMY), where both male and female mice show a negative correlation between latency times and activated cell counts. These results are coherent with the role of the BMA in fear memory[2] and of the sAMY in supporting affective evaluation and learning.[45,46] Interestingly, female mice show significant correlation in the ventral pallidum (PALv). This finding, together with recent literature,[9] underlines an important yet hitherto neglected role of the PALv in fear memory. The olfactory area (OLF) posterior amygdalar nucleus (PA), an amygdalar region well known for its role in fear memory[42,47–49]; the periventricular zone (PVZ), which is an important autonomic control center in response to stress exposure[50]; and the median eminence (ME) and midbrain (MB) are instead characterized by a distinct anti-correlation with step-through latency.

In males, latency times 7 days after training show strong correlation with the posterior parietal association area (PTLp) and anti-correlation with the lateral septal complex (LSX). This finding confirms the involvement of the LSX in memory and emotional responses: indeed, previous reports show that this region is activated during aversive situations[8,51,52] and projects to brain regions involved in behavioral and cardiovascular responses to aversive stimuli.[53] In addition, the involvement of the globus pallidus, already observed 24 h after training, is confirmed. Female subjects show a completely different pattern of correlation with behavior. Latency times are significantly anti-correlated with activation of the FRP and the PL, areas that are significant sexually dysmorphic in the PLS analysis too. Notably, a recent study highlighted the role of the FRP in decision-making as that of the whole prefrontal region.[54] The correlation of latency times is positive also in the OLF RHP and in most amygdalar regions, areas that are well known to be involved in fear.[42,47–49] Interestingly, at 7 day retrieval, the PA shows an opposite correlation between sexes. Focusing on the hippocampal area, we observe a general trend of anti-correlation in both sexes that, however, is restricted to the CA in females and to the DG in males.

Network analysis shows strong sexual dimorphism in the evolution of functional connectivity

Widely accepted theories affirm that memory is distributed across multiple brain regions that are functionally connected.[15,55] To estimate average functional connectivity in different behavioral groups, we performed a Pearson cross-correlation analysis between normalized activation counts of different brain areas, among subjects of the same experimental group (Figure S2). To consider potential effects of the finite accuracy of the cell detection algorithm, we performed Monte Carlo simulations of cross-correlations in the presence of noise in activation counts. We found significant variability in correlation strength (Figure S3A); however, stronger (anti-)correlations appeared more stable, as the average standard deviation of correlations with p <0.05 (anti-)correlations is close to 0.05. Thus, the correlations and anti-correlations with p <0.05 reasonably identify those that will not exceed p = 0.1, taking into account noise in activation count. Considering only those (anti-)correlations (Figure S3B), we identified a network of brain areas that show a statistically significant tendency to be active together (for correlations) or in a mutually exclusive manner (for anti-correlations) (Figure 4). Thus, brain areas are the nodes of this network, while the edges represent putative functional connections identified by super-threshold cross-correlation.

Interestingly, female and male activity networks showed a different evolution over time (Figure 4A). In order to quantitatively analyze differences in organization, we compared a number of connectivity features in male and female networks. The distribution of nodes degree[56] was similar for the two sexes at both training and test 7 days, while 24 h after training, the female network was characterized by a large increase in connectivity (Figure 4B). Interestingly, in male mice, we observe a decrease of the relative contribution of positive correlations from training (83%) to test 7 days (64%) with a minimum at test 24 h (61%), while females show the opposite trend (53% at training, 63% at test 7 days) with a peak at 24 h after training (76%; Figure S4A). If we restrict our analysis to the isocortex, we observe that the intraregional connectivity (normalized on the global average node degree) follows a trend similar to the global connectivity. These results suggests that engram migration to the cortex, which is a cornerstone of system consolidation theories,[25,55,57] occurs with different spatiotemporal patterns in males and females but that both sexes tend to converge to the same network structure (Figure S4B).

The sexual dimorphism observed in network evolution is confirmed by small-world analysis. For each network, we evaluated the small-world coefficient σ of the giant component (i.e., isolated nodes were not considered), defined as (C/Cr)/(L/Lr), with C and L being the average clustering coefficient and the average shortest path lengths of the graph, respectively. Cr and Lr are the corresponding values for an equivalent random graph. σ is equal to one in graphs with a structure similar to random ones, whereas it is higher than one when the network is small world, i.e., when non-neighboring regions are separated by a small number of steps compared with a random network. At training and test 7 days, we observed a network presenting small-word features for both sexes. Conversely, the network of the 24 h group largely resembles a random graph for the female group but not for the male group (Figure 4C). This finding supports the hypothesis that the circuitry of male and female mice evolves toward an organized cortical network following different pathways.

Hubs of functional connectivity change over time in a sexually dimorphic manner

In addition to global properties of the connectivity graph, we assessed the role of different nodes by measuring their degree and betweenness. The degree of a node is the number of connections it has with the other nodes in the network, whereas
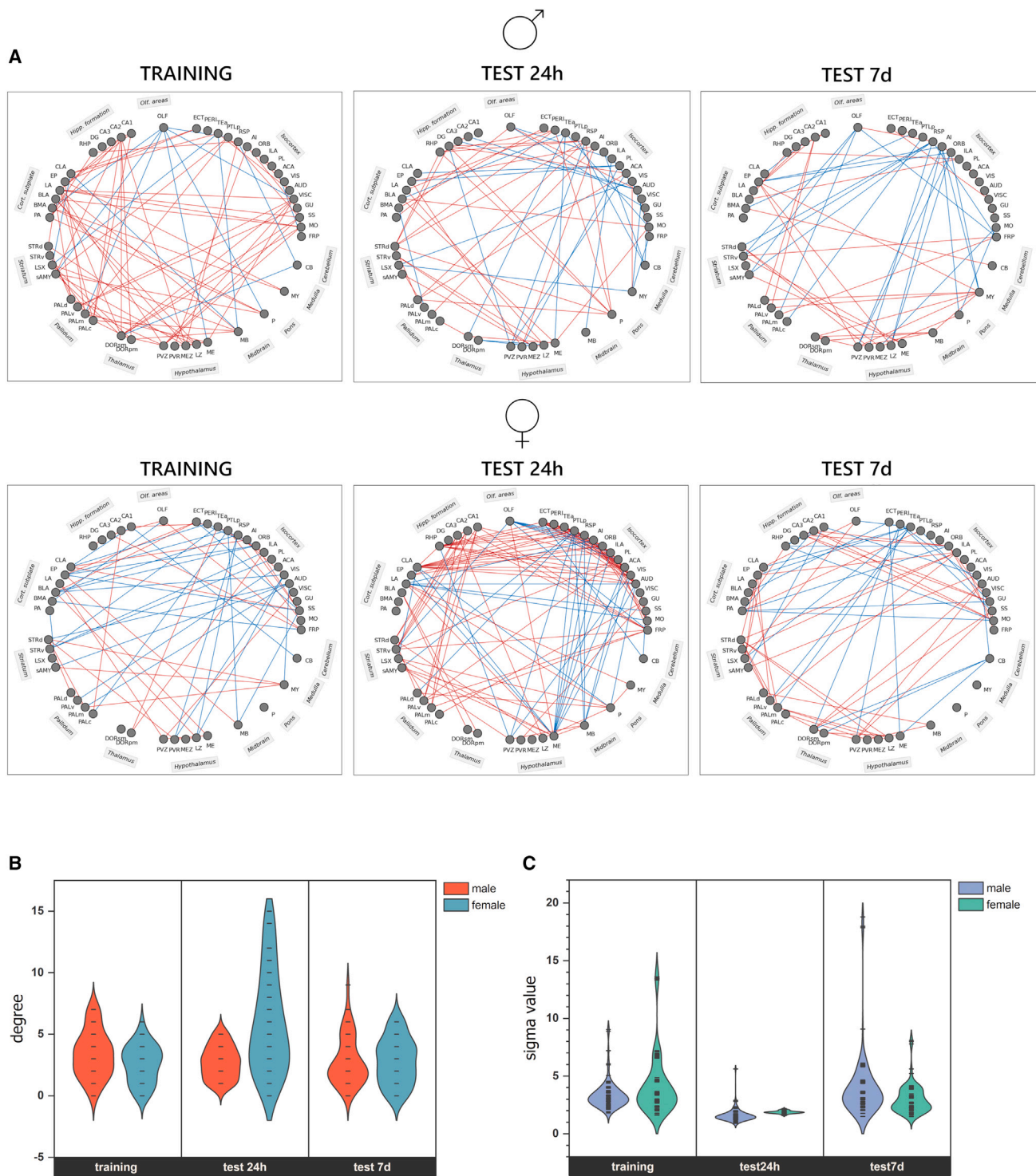
Figure 4. Fear memory networks in male and female mice

(A) Network graphs were generated by considering only the strongest correlations (see STAR Methods). Gray circles represent the 48 selected regions (listed in Table 1). The lines between the nodes represent significant positive (red) or negative (blue) correlations (see STAR Methods for thresholding details).

(B) Violin plot of the connectivity of all the nodes in the networks shown in (A).

(C) Violin plots of sigma values for the networks shown in (A), calculated for N = 100 generations of random graphs (see STAR Methods).
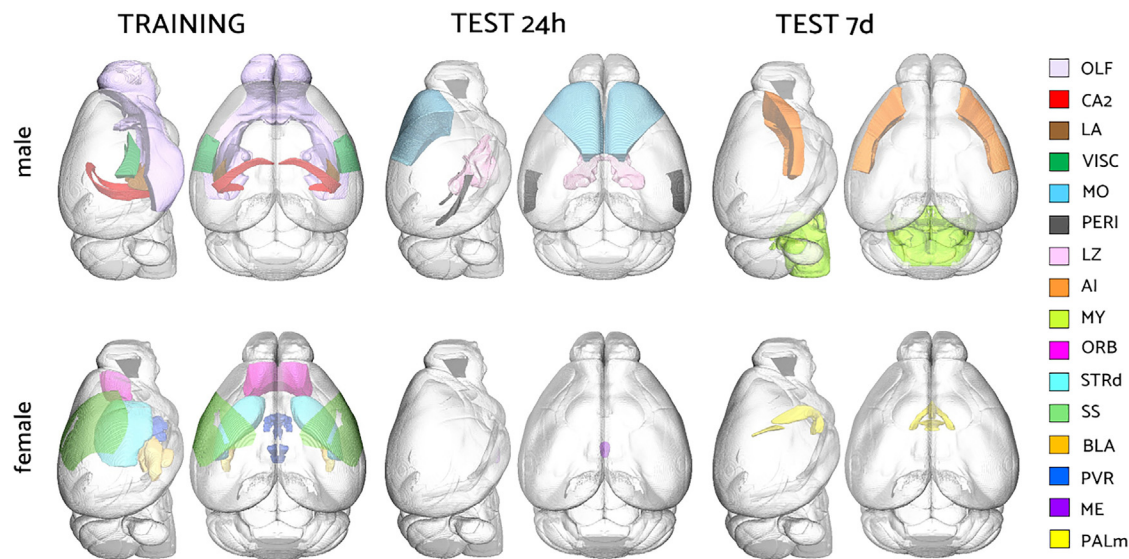
Figure 5. Spatiotemporal evolution of functional connectivity hubs
3D rendering of a reference mouse brain where hubs of specific time points are depicted with different colors. At 24 h after training, the functional hub for the female group is represented by the ME. The ME is a small nucleus in the brain's center, here colored in violet. Each color represents a single brain region according to Table 1.

betweenness is defined as the probability of finding the node in the shortest path between any randomly chosen pair of nodes in the network. In other words, the degree is a direct measure of the influence of the node in the network (the higher the degree, the more the activity of the node correlates with that of other nodes), while the betweenness states the importance of the node for connectivity (i.e., if a node with high betweenness is removed, many paths between other nodes are cut). We considered as hubs those nodes that are simultaneously above the 80th percentile of degree and betweenness values (Figure S5).

We found that region involvement as a hub shows distinct time evolution in males and females (Figure 5; Table 2). In male subjects, we observed a hub evolution involving both cortical and subcortical areas. At the subcortical level, hubs move along a rostro-caudal axis, from the CA2 and the OLF at training to the hypothalamic lateral zone (LZ) at test 24 h and to the medulla (MY) at test 7 days. At the cortical level, we observe a transition from sensorimotor cortices (VISC at training and somatomotor area [MO] at test 24 h) to associative areas (AI). This migration toward the associative cortex is in line with the standard theory of memory consolidation.[2] Conversely, in female subjects, network hubs persist in subcortical regions across the entire time span investigated, moving from the basolateral amygdalar nucleus (BLA) and the striatum dorsal region (STRd) at training to the ME at test 24 h and the medial palladium (PALm) at test 7days. At training, we found also two cortical hubs (SS and ORB). The SS is a region processing proprioceptive stimuli, suggesting a role of this hub in elaborating the unconditioned stimulus (foot shock).

These results are partially in line with the PLS analysis. Indeed, several hubs are significantly more active in their respective sex, including the VISC and the periventricular region (PVR) at training, the ME, the MO, and the PERI at test 24 h, and the

PALm at test 7 days. Notably, at training, we observe hubs that are more recruited in the other sex, i.e., the CA2 is a hub for males (but is more recruited in females) and the SS is a hub for females (but is more recruited in males). Hubs at test 7 days for males do not show any preferential activation between sexes (Figure 2C).

Finally, we observed a common feature of both male and female networks: hub regions at training at test 7 days are distinct from areas where activation significantly correlates with step-through latency times. Conversely, at test 24 h, the PERI and the ME appear as hubs for males and females, respectively, and also show negative correlation between neuronal activation and latency times (Figure 3). Overall, these results suggest that hubs do not directly modulate behavior but rather orchestrate downstream circuits mediating behavioral output.

DISCUSSION

Memory, as many other cognitive processes, involves complex neuronal circuits that are distributed across the entire brain and change with time.[58] Thus, from a technical perspective, it is important to have tools that allow scalable, unbiased, and quantitative analysis of brain activity at the organ level yet with single-cell resolution. The classical procedure to reach this aim consists in serial sectioning of the tissue, immunostaining against cFos (or another IEG), and analysis of tissue slices.[59] Although this protocol has been exploited to characterize the networks recruited during contextual[25] or tone fear conditioning,[23] a massive amount of work is required to process each murine brain and thus is impractical for routine use in many laboratories. Automated 3D imaging, such as serial two-photon sectioning (STP)[60] and LSM,[61] has emerged in

Table 2. Putative functional connectivity hubs

	Training	Test 24 h	Test 7 days
Male	LA, CA2, OLF, VISC	MO, PERI, LZ	MY, AI
Female	BLA, STRd, SS, PVR, ORB	ME	PALm

Functional connectivity hubs in male and female mice at different time points, defined as those regions in the top 20th percentile of both betweenness and degree.

the last decade as a potential game changer for whole-brain analysis at the cellular level, and indeed, it has been exploited to map neuronal activation in different contexts,[14,62] including fear memory.[15,26] However, STP is usually employed in a sampling scheme, failing to cover the entire tissue volume.[62] On the other hand, LSM-based pipelines, like ClearMap, are typically limited to a resolution of several μm per voxel, preventing their use in densely labeled regions (Figure 1). Here, we presented BRANT, a combination of high-resolution LSM and scalable computational analysis. On the optics side, the use of RAPID autofocusing guarantees high contrast and resolution across the entire sample.[28] On the image processing side, the architecture provided by ZetaStitcher allows programmatic access to small chunks of data in an otherwise extra-large tissue volume (several teravoxels) for subsequent quantification, and the use of a deep-learning method for cell detection (bcFind) enables superior accuracy when applied to neurons labeled in their entirety (compared to nuclear staining of anti-cFos immunohistochemistry). In this study, we quantitatively compared BRANT with ClearMap, one of the most widely used tool for automated cell detection. Several other tools have emerged in the last decade for this task (Table S3). However, each of them shows intrinsic limitations that might prevent its application to a large-scale brain-wide study like the one presented here. On the one hand, a large number of tools have been designed for small imaging datasets and lack the computational structure to scale properly to the TB-sized images.[14,63–70] On the other hand, quantification algorithms validated on large-scale datasets are either based on standard image filters,[14,66] are designed to work with simple nuclear staining, or need an additional background channel.[69] Overall, the innovations introduced in this work enable routine and scalable analyses that were not possible using previously reported methodology. Importantly, BRANT is based on fully open-source software available on GitHub and can thus be used and improved by the entire community in a collaborative spirit.

The lack of scalable methods for whole-brain mapping has limited the analysis of brain-wide activation patterns in fear memory to a handful of studies.[6,23–26] Most reports about fear memory refer to one or few nuclei or areas. Consequently, the obtained results are specific to those neuronal regions, which in turn makes it difficult to form an overview when integrating the data. Indeed, small changes in the experimental setting (from the behavioral task to the age and sex of animals) can lead to contrasting outcomes, making it difficult to obtain a comprehensive view of brain circuits underlying memory formation, consolidation, and retrieval. Additionally, this problem is even more accentuated considering the limited literature about female subjects and sex differences. Actually, sexual dimor-

phism studies may improve the translationability in fear memory research, as females are two times more likely than men to experience any anxiety-related condition.[71] Since fear is considered one of the best conserved emotional mechanism,[2,71] it is likely that differences in neuronal activation patterns between sexes observed in animals are reflected in humans. For this reason, it is essential for researchers to include females in both human and animal studies.

The majority of previous studies about sexual dimorphisms have mainly highlighted differences in brain anatomy[62,72–74] and in cellular physiology.[75] The identification of these anatomical or molecular differences is a useful starting point for the comprehension of neural circuits underlying sex-specific behaviors, but brain-scale functional studies are needed to disentangle the shape of different circuits recruited during the evolution of aversive memory.

In this context, our study demonstrated that fear memory is associated with the recruitment of sex-specific networks. It is noteworthy how this difference is emphasized during the 24 h retrieval, suggesting that female mice augment their brain-wide functional connectivity state to evolve more quickly to a network similar to the starting conditions, with preferential involvement of different brain regions.

Interestingly, the functional network of male mice changes over time, recruiting distinct regions but not increasing the number of nodes and connections at each memory phase. Overall, these data suggest that fear learning and retrieval are mediated by distinct subsystems in the two sexes, challenging the use of a male-predominant literature for understanding aversive memory in females. Generally, this study could pave the way for a better understanding of those neuro-psychiatric disorders that exhibit sex differences in lifetime prevalence such as PTSD, anxiety, and depression.[76–80]

Here, BRANT was applied to understand the time evolution of brain circuits underpinning fear memory in an IA paradigm with a mild foot shock. Due to the limited number of whole-brain studies about fear memory, and the lack of involvement of female subjects, comparing our results with previous reports[23,25] is not straightforward because fear memory can be assessed in rodents by using diverse behavioral tasks. Indeed, the IA behavioral paradigm presented here might recruit a different circuitry with respect to context or auditory fear conditioning since decision-making—to step through the gate toward the dark compartment—is an important component, absent in the above mentioned paradigms. In addition, using a mild foot shock (0.3 mA), we explored an aversive rather than traumatic memory. Nevertheless, our results confirm the unified engram complex theory,[15] proving that memory evolution recruits dynamical networks across the entire brain.

In this fragmented context—both on the brain region studied and on the behavioral task used—the scalable and comprehensive analysis enabled by BRANT can play an important role. Indeed, this pipeline exploits well-described protocols and open-source software, offering to any lab the possibility to perform whole-brain activation analysis at high throughput, allowing cell-resolution brain mapping on behavioral cohorts. Here, this method highlighted a sexual dimorphism in the evolution of fear memory, but it is readily

adaptable for broader applications such as drug discovery or other biological purposes. The advantage of using micrometer resolution on a brain-wide scale and 3D automated analysis could revolutionize the way of studying brain connectivity and functions.

Limitations of the study

Due to the pharmacokinetics of 4-OHT, TRAP-mediated recombination covers a time frame of about 6 h, larger than the behaviorally relevant timescale.[16] Thus, not all the neurons labeled are recruited by the behavioral test. In addition, c-Fos itself tags only a part of the activated neurons.[81]

The 3D U-Net used for cell detection has very good performances when compared with other methods used in the field (Figure 1C), but in absolute terms, the F1 score could be significantly improved. The use of more advanced architectures, like residual models[82] or attention mechanisms,[83] can be explored to boost accuracy.

Registration to the reference atlas has an accuracy of about 300 μm, which is insufficient to compare neuronal activation between small structures (e.g., cortical layers). To solve this aim, future studies might employ reference atlases built upon light-sheet imaging,[84] providing a template closer to our images in terms of shape and contrast.

Limited accuracy of cell detection and atlas registration might introduce errors in downstream analysis. Only a simplified analysis of the effects of this uncertainty is reported here. A thorough study of how counting and registration errors are propagated is beyond the scope of this resource.

STAR★METHODS

Detailed methods are provided in the online version of this paper and include the following:

- KEY RESOURCES TABLE
- RESOURCE AVAILABILITY
  - Lead contact
  - Materials availability
  - Data and code availability
- EXPERIMENTAL MODEL AND SUBJECT DETAILS
- METHOD DETAILS
  - Animals
  - Behavioral task
  - Delivery of 4-OHT
  - Ex-vivo brain processing
  - Light-sheet microscopy
  - Image analysis
  - Whole-brain cell detection
  - Spatial registration to reference atlas
- QUANTIFICATION AND STATISTICAL ANALYSIS
  - Partial least square analysis
  - Functional network generation

SUPPLEMENTAL INFORMATION

Supplemental information can be found online at https://doi.org/10.1016/j.celrep.2023.112908.

AUTHOR CONTRIBUTIONS

A.F. performed animal experiments and prepared and imaged samples; L.S. conceived the research and coordinated the project; M.B.P. designed behavioral experiments; G.M. and C.C. developed BRANT-related software; F.S.P. contributed advanced imaging tools; I.C. contributed advanced clearing methods; L.C. and D.F. performed network analysis; B.A.S., A.F., and L.S. analyzed data; A.F. and L.S. wrote the manuscript with contribution from all other authors.

DECLARATION OF INTERESTS

The authors declare no competing interests.

INCLUSION AND DIVERSITY

We support inclusive, diverse, and equitable conduct of research.

REFERENCES

1. Kindt, M. (2014). A behavioural neuroscience perspective on the aetiology and treatment of anxiety disorders. Behav. Res. Ther. *62*, 24–36.

2. Izquierdo, I., Furini, C.R.G., and Myskiw, J.C. (2016). Fear Memory. Physiol. Rev. *96*, 695–750.

3. Josselyn, S.A., Köhler, S., and Frankland, P.W. (2015). Finding the engram. Nat. Rev. Neurosci. *16*, 521–534.

4. Josselyn, S.A., and Frankland, P.W. (2018). Memory Allocation: Mechanisms and Function. Annu. Rev. Neurosci. *41*, 389–413.

5. Johansen, J.P., Cain, C.K., Ostroff, L.E., and LeDoux, J.E. (2011). Molecular Mechanisms of Fear Learning and Memory. Cell *147*, 509–524.

6. Tonegawa, S., Morrissey, M.D., and Kitamura, T. (2018). The role of engram cells in the systems consolidation of memory. Nat. Rev. Neurosci. *19*, 485–498.

7. Orsini, C.A., and Maren, S. (2012). Neural and cellular mechanisms of fear and extinction memory formation. Neurosci. Biobehav. Rev. *36*, 1773–1802.

8. Pezzone, M.A., Lee, W.-S., Hoffman, G.E., and Rabin, B.S. (1992). Induction of c-Fos immunoreactivity in the rat forebrain by conditioned and unconditioned aversive stimuli. Brain Res. *597*, 41–50.

9. Moaddab, M., Ray, M.H., and McDannald, M.A. (2021). Ventral pallidum neurons dynamically signal relative threat. Commun. Biol. *4*, 43.

10. Silva, B.A., Astori, S., Burns, A.M., Heiser, H., van den Heuvel, L., Santoni, G., Martinez-Reza, M.F., Sandi, C., and Gräff, J. (2021). A thalamo-amygdalar circuit underlying the extinction of remote fear memories. Nat. Neurosci. *24*, 964–974.

11. Chung, K., Wallace, J., Kim, S.Y., Kalyanasundaram, S., Andalman, A.S., Davidson, T.J., Mirzabekov, J.J., Zalocusky, K.A., Mattis, J., Denisin, A.K., et al. (2013). Structural and molecular interrogation of intact biological systems. Nature *497*, 332–337.

12. Renier, N., Wu, Z., Simon, D.J., Yang, J., Ariel, P., and Tessier-Lavigne, M. (2014). iDISCO: A Simple, Rapid Method to Immunolabel Large Tissue Samples for Volume Imaging. Cell *159*, 896–910.

13. Susaki, E.A., Tainaka, K., Perrin, D., Kishino, F., Tawara, T., Watanabe, T.M., Yokoyama, C., Onoe, H., Eguchi, M., Yamaguchi, S., et al. (2014). Whole-Brain Imaging with Single-Cell Resolution Using Chemical Cocktails and Computational Analysis. Cell *157*, 726–739.

14. Renier, N., Adams, E.L., Kirst, C., Wu, Z., Azevedo, R., Kohl, J., Autry, A.E., Kadiri, L., Umadevi Venkataraju, K., Zhou, Y., et al. (2016). Mapping of Brain Activity by Automated Volume Analysis of Immediate Early Genes. Cell *165*, 1789–1802.

15. Roy, D.S., Park, Y.G., Kim, M.E., Zhang, Y., Ogawa, S.K., DiNapoli, N., Gu, X., Cho, J.H., Choi, H., Kamentsky, L., et al. (2022). Brain-wide mapping reveals that engrams for a single memory are distributed across multiple brain regions. Nat. Commun. *13*, 1799.

16. Guenthner, C.J., Miyamichi, K., Yang, H.H., Heller, H.C., and Luo, L. (2013). Permanent Genetic Access to Transiently Active Neurons via TRAP: Targeted Recombination in Active Populations. Neuron *78*, 773–784.

17. DeNardo, L.A., Liu, C.D., Allen, W.E., Adams, E.L., Friedmann, D., Fu, L., Guenthner, C.J., Tessier-Lavigne, M., and Luo, L. (2019). Temporal evolution of cortical ensembles promoting remote memory retrieval. Nat. Neurosci. *22*, 460–469.

18. Denny, C.A., Kheirbek, M.A., Alba, E.L., Tanaka, K.F., Brachman, R.A., Laughman, K.B., Tomm, N.K., Turi, G.F., Losonczy, A., and Hen, R. (2014). Hippocampal Memory Traces Are Differentially Modulated by Experience, Time, and Adult Neurogenesis. Neuron *83*, 189–201.

19. Franceschini, A., Costantini, I., Pavone, F.S., and Silvestri, L. (2020). Dissecting Neuronal Activation on a Brain-Wide Scale With Immediate Early Genes. Front. Neurosci. *14*, 569517.

20. Charak, R., Armour, C., Elklit, A., Angmo, D., Elhai, J.D., and Koot, H.M. (2014). Factor structure of PTSD, and relation with gender in trauma survivors from India. Eur. J. Psychotraumatol. *5*, 25547.

21. Christiansen, D.M., and Hansen, M. (2015). Accounting for sex differences in PTSD: A multi-variable mediation model. Eur. J. Psychotraumatol. *6*, 26068.

22. Zucker, I., and Beery, A.K. (2010). Males still dominate animal studies. Nature *465*, 690.

23. Cho, J.-H., Rendall, S.D., and Gray, J.M. (2017). Brain-wide maps of *Fos* expression during fear learning and recall. Learn. Mem. *24*, 169–181.

24. Vetere, G., Kenney, J.W., Tran, L.M., Xia, F., Steadman, P.E., Parkinson, J., Josselyn, S.A., and Frankland, P.W. (2017). Chemogenetic Interrogation of a Brain-wide Fear Memory Network in Mice. Neuron *94*, 363–374.e4.

25. Wheeler, A.L., Teixeira, C.M., Wang, A.H., Xiong, X., Kovacevic, N., Lerch, J.P., McIntosh, A.R., Parkinson, J., and Frankland, P.W. (2013). Identification of a Functional Connectome for Long-Term Fear Memory in Mice. PLoS Comput. Biol. *9*, e1002853.

26. Bonapersona, V., Schuler, H., Damsteegt, R., Adolfs, Y., Pasterkamp, R.J., van den Heuvel, M.P., Joëls, M., and Sarabdjitsingh, R.A. (2022). The mouse brain after foot shock in four dimensions: Temporal dynamics at a single-cell resolution. Proc. Natl. Acad. Sci. USA *119*, e2114002119.

27. Costantini, I., Ghobril, J.P., Di Giovanna, A.P., Allegra Mascaro, A.L., Silvestri, L., Müllenbroich, M.C., Onofri, L., Conti, V., Vanzi, F., Sacconi, L., et al. (2015). A versatile clearing agent for multi-modal brain imaging. Sci. Rep. *5*, 9808.

28. Silvestri, L., Müllenbroich, M.C., Costantini, I., Di Giovanna, A.P., Mazzamuto, G., Franceschini, A., Kutra, D., Kreshuk, A., Checcucci, C., Toresano, L.O., et al. (2021). Universal autofocus for quantitative volumetric microscopy of whole mouse brains. Nat. Methods *18*, 953–958.

29. Frasconi, P., Silvestri, L., Soda, P., Cortini, R., Pavone, F.S., and Iannello, G. (2014). Large-scale automated identification of mouse brain cells in confocal light sheet microscopy images. Bioinformatics *30*, i587–i593.

30. Di Giovanna, A.P., Credi, C., Franceschini, A., Müllenbroich, M.C., Silvestri, L., and Pavone, F.S. (2019). Tailored Sample Mounting for Light-Sheet Fluorescence Microscopy of Clarified Specimens by Polydimethylsiloxane Casting. Front. Neuroanat. *13*, 35.

31. Müllenbroich, M.C., Silvestri, L., Onofri, L., Costantini, I., Hoff, M.V., Sacconi, L., Iannello, G., and Pavone, F.S. (2015). Comprehensive optical and data management infrastructure for high-throughput light-sheet microscopy of whole mouse brains. Neurophoton *2*, 041404.

32. Ronneberger, O., Fischer, P., and Brox, T.U.-N. (2015). Convolutional Networks for Biomedical Image Segmentation. In Medical Image Computing and Computer-Assisted Intervention – MICCAI 2015, *9351*, N. Navab, J. Hornegger, W.M. Wells, and A.F. Frangi, eds. (Springer International Publishing), pp. 234–241.

33. Avants, B.B., Tustison, N.J., Song, G., Cook, P.A., Klein, A., and Gee, J.C. (2011). A reproducible evaluation of ANTs similarity metric performance in brain image registration. Neuroimage *54*, 2033–2044.

34. Canto-de-Souza, L., and Mattioli, R. (2016). The consolidation of inhibitory avoidance memory in mice depends on the intensity of the aversive stimulus: The involvement of the amygdala, dorsal hippocampus and medial prefrontal cortex. Neurobiol. Learn. Mem. *130*, 44–51.

35. Benetti, F., Furini, C.R.G., de Carvalho Myskiw, J., Provensi, G., Passani, M.B., Baldi, E., Bucherelli, C., Munari, L., Izquierdo, I., and Blandina, P. (2015). Histamine in the basolateral amygdala promotes inhibitory avoidance learning independently of hippocampus. Proc. Natl. Acad. Sci. USA *112*, E2536–E2542.

36. Krishnan, A., Williams, L.J., McIntosh, A.R., and Abdi, H. (2011). Partial Least Squares (PLS) methods for neuroimaging: A tutorial and review. Neuroimage *56*, 455–475.

37. Bucci, D.J., and Robinson, S. (2014). Toward a conceptualization of retro-hippocampal contributions to learning and memory. Neurobiol. Learn. Mem. *116*, 197–207.

38. Smith, D.M., and Bulkin, D.A. (2014). The form and function of hippocampal context representations. Neurosci. Biobehav. Rev. *40*, 52–61.

39. Ray, M.H., Russ, A.N., Walker, R.A., and McDannald, M.A. (2020). The Nucleus Accumbens Core is Necessary to Scale Fear to Degree of Threat. J. Neurosci. *40*, 4750–4760.

40. Giustino, T.F., and Maren, S. (2015). The Role of the Medial Prefrontal Cortex in the Conditioning and Extinction of Fear. Front. Behav. Neurosci. *9*, 298.

41. Kent, B.A., and Brown, T.H. (2012). Dual functions of perirhinal cortex in fear conditioning. Hippocampus *22*, 2068–2079.

42. Sacchetti, B., Baldi, E., Lorenzini, C.A., and Bucherelli, C. (2002). Cerebellar role in fear-conditioning consolidation. Proc. Natl. Acad. Sci. USA *99*, 8406–8411.

43. Ivashkina, O.I., Gruzdeva, A.M., Roshchina, M.A., Toropova, K.A., and Anokhin, K.V. (2021). Imaging of C-fos Activity in Neurons of the Mouse Parietal Association Cortex during Acquisition and Retrieval of Associative Fear Memory. IJMS *22*, 8244.

44. Tasaka, G.I., Feigin, L., Maor, I., Groysman, M., DeNardo, L.A., Schiavo, J.K., Froemke, R.C., Luo, L., and Mizrahi, A. (2020). The Temporal

Association Cortex Plays a Key Role in Auditory-Driven Maternal Plasticity. Neuron *107*, 566–579.e7.

45. Ehrlich, I., Humeau, Y., Grenier, F., Ciocchi, S., Herry, C., and Lüthi, A. (2009). Amygdala Inhibitory Circuits and the Control of Fear Memory. Neuron *62*, 757–771.

46. Goode, T.D., and Maren, S. (2017). Role of the bed nucleus of the stria terminalis in aversive learning and memory. Learn. Mem. *24*, 480–491.

47. Fareri, D.S., and Tottenham, N. (2016). Effects of early life stress on amygdala and striatal development. Dev. Cogn. Neurosci. *19*, 233–247.

48. Hoffman, A.N., Lorson, N.G., Sanabria, F., Foster Olive, M., and Conrad, C.D. (2014). Chronic stress disrupts fear extinction and enhances amygdala and hippocampal Fos expression in an animal model of post-traumatic stress disorder. Neurobiol. Learn. Mem. *112*, 139–147.

49. Kitanishi, T., and Matsuo, N. (2017). Organization of the Claustrum-to-Entorhinal Cortical Connection in Mice. J. Neurosci. *37*, 269–280.

50. Herman, J.P., and Tasker, J.G. (2016). Paraventricular Hypothalamic Mechanisms of Chronic Stress Adaptation. Front. Endocrinol. *7*, 137.

51. Beck, C.H., and Fibiger, H.C. (1995). Conditioned fear-induced changes in behavior and in the expression of the immediate early gene c-fos: with and without diazepam pretreatment. J. Neurosci. *15*, 709–720.

52. Duncan, G.E., Johnson, K.B., and Breese, G.R. (1993). Topographic patterns of brain activity in response to swim stress: assessment by 2-deoxyglucose uptake and expression of Fos-like immunoreactivity. J. Neurosci. *13*, 3932–3943.

53. LeDoux, J.E., Iwata, J., Cicchetti, P., and Reis, D.J. (1988). Different projections of the central amygdaloid nucleus mediate autonomic and behavioral correlates of conditioned fear. J. Neurosci. *8*, 2517–2529.

54. Lv, C., Wang, Q., Chen, C., Xue, G., and He, Q. (2021). Activation patterns of the dorsal medial prefrontal cortex and frontal pole predict individual differences in decision impulsivity. Brain Imaging Behav. *15*, 421–429.

55. Frankland, P.W., and Bontempi, B. (2005). The organization of recent and remote memories. Nat. Rev. Neurosci. *6*, 119–130.

56. Hallquist, M.N., and Hillary, F.G. (2019). Graph theory approaches to functional network organization in brain disorders: A critique for a brave new small-world. Netw. Neurosci. *3*, 1–26.

57. Albo, Z., and Gräff, J. (2018). The mysteries of remote memory. Phil. Trans. R. Soc. B *373*, 20170029.

58. Herry, C., and Johansen, J.P. (2014). Encoding of fear learning and memory in distributed neuronal circuits. Nat. Neurosci. *17*, 1644–1654.

59. Kim, Y., Venkataraju, K.U., Pradhan, K., Mende, C., Taranda, J., Turaga, S.C., Arganda-Carreras, I., Ng, L., Hawrylycz, M.J., Rockland, K.S., et al. (2015). Mapping Social Behavior-Induced Brain Activation at Cellular Resolution in the Mouse. Cell Rep. *10*, 292–305.

60. Ragan, T., Kadiri, L.R., Venkataraju, K.U., Bahlmann, K., Sutin, J., Taranda, J., Arganda-Carreras, I., Kim, Y., Seung, H.S., and Osten, P. (2012). Serial two-photon tomography for automated ex vivo mouse brain imaging. Nat. Methods *9*, 255–258.

61. Mertz, J. (2011). Optical sectioning microscopy with planar or structured illumination. Nat. Methods *8*, 811–819.

62. Kim, Y., Yang, G.R., Pradhan, K., Venkataraju, K.U., Bota, M., García Del Molino, L.C., Fitzgerald, G., Ram, K., He, M., Levine, J.M., et al. (2017). Brain-wide Maps Reveal Stereotyped Cell-Type-Based Cortical Architecture and Subcortical Sexual Dimorphism. Cell *171*, 456–469.e22.

63. Barry, D.J., Gerri, C., Bell, D.M., D'Antuono, R., and Niakan, K.K. (2022). GIANI – open-source software for automated analysis of 3D microscopy images. J. Cell Sci. *135*, jcs259511.

64. Berg, S., Kutra, D., Kroeger, T., Straehle, C.N., Kausler, B.X., Haubold, C., Schiegg, M., Ales, J., Beier, T., Rudy, M., et al. (2019). ilastik: interactive machine learning for (bio)image analysis. Nat. Methods *16*, 1226–1232.

65. Hodneland, E., Kögel, T., Frei, D.M., Gerdes, H.-H., and Lundervold, A. (2013). CellSegm - a MATLAB toolbox for high-throughput 3D cell segmentation. Source Code Biol. Med. *8*, 16.

66. Murakami, T.C., Mano, T., Saikawa, S., Horiguchi, S.A., Shigeta, D., Baba, K., Sekiya, H., Shimizu, Y., Tanaka, K.F., Kiyonari, H., et al. (2018). A three-dimensional single-cell-resolution whole-brain atlas using CUBIC-X expansion microscopy and tissue clearing. Nat. Neurosci. *21*, 625–637.

67. Shuvaev, S.A., Lazutkin, A.A., Kedrov, A.V., Anokhin, K.V., Enikolopov, G.N., and Koulakov, A.A. (2017). DALMATIAN: An Algorithm for Automatic Cell Detection and Counting in 3D. Front. Neuroanat. *11*, 117.

68. Stirling, D.R., Swain-Bowden, M.J., Lucas, A.M., Carpenter, A.E., Cimini, B.A., and Goodman, A. (2021). CellProfiler 4: improvements in speed, utility and usability. BMC Bioinf. *22*, 433.

69. Tyson, A.L., Rousseau, C.V., Niedworok, C.J., Keshavarzi, S., Tsitoura, C., Cossell, L., Strom, M., and Margrie, T.W. (2021). A deep learning algorithm for 3D cell detection in whole mouse brain image datasets. PLoS Comput. Biol. *17*, e1009074.

70. Yates, S.C., Groeneboom, N.E., Coello, C., Lichtenthaler, S.F., Kuhn, P.H., Demuth, H.U., Hartlage-Rübsamen, M., Roßner, S., Leergaard, T., Kreshuk, A., et al. (2019). QUINT: Workflow for Quantification and Spatial Analysis of Features in Histological Images From Rodent Brain. Front. Neuroinform. *13*, 75.

71. Flores, Á., Fullana, M.À., Soriano-Mas, C., and Andero, R. (2018). Lost in translation: how to upgrade fear memory research. Mol. Psychiatry *23*, 2122–2132.

72. Bayless, D.W., and Shah, N.M. (2016). Genetic dissection of neural circuits underlying sexually dimorphic social behaviours. Phil. Trans. R. Soc. B *371*, 20150109.

73. Simerly, R.B. (2002). Wired for Reproduction: Organization and Development of Sexually Dimorphic Circuits in the Mammalian Forebrain. Annu. Rev. Neurosci. *25*, 507–536.

74. Cachero, S., Ostrovsky, A.D., Yu, J.Y., Dickson, B.J., and Jefferis, G.S.X.E. (2010). Sexual Dimorphism in the Fly Brain. Curr. Biol. *20*, 1589–1601.

75. Florido, A., Velasco, E.R., Soto-Faguás, C.M., Gomez-Gomez, A., Perez-Caballero, L., Molina, P., Nadal, R., Pozo, O.J., Saura, C.A., and Andero, R. (2021). Sex differences in fear memory consolidation via Tac2 signaling in mice. Nat. Commun. *12*, 2496.

76. Bangasser, D.A., and Valentino, R.J. (2014). Sex differences in stress-related psychiatric disorders: Neurobiological perspectives. Front. Neuroendocrinol. *35*, 303–319.

77. Smith, K.M., and Dahodwala, N. (2014). Sex differences in Parkinson's disease and other movement disorders. Exp. Neurol. *259*, 44–56.

78. Werling, D.M., and Geschwind, D.H. (2013). Sex differences in autism spectrum disorders. Curr. Opin. Neurol. *26*, 146–153.

79. Davies, W. (2014). Sex differences in Attention Deficit Hyperactivity Disorder: Candidate genetic and endocrine mechanisms. Front. Neuroendocrinol. *35*, 331–346.

80. Li, R., and Singh, M. (2014). Sex differences in cognitive impairment and Alzheimer's disease. Front. Neuroendocrinol. *35*, 385–403.

81. Sun, X., Bernstein, M.J., Meng, M., Rao, S., Sørensen, A.T., Yao, L., Zhang, X., Anikeeva, P.O., and Lin, Y. (2020). Functionally Distinct Neuronal Ensembles within the Memory Engram. Cell *181*, 410–423.e17.

82. He, K., Zhang, X., Ren, S., and Sun, J. (2015). Deep Residual Learning for Image Recognition. https://doi.org/10.48550/ARXIV.1512.03385.

83. Wang, Q., Wu, B., Zhu, P., Li, P., Zuo, W., and Hu, Q. (2019). ECA-Net: Efficient Channel Attention for Deep Convolutional Neural Networks. https://doi.org/10.48550/ARXIV.1910.03151.

84. Perens, J., Salinas, C.G., Skytte, J.L., Roostalu, U., Dahl, A.B., Dyrby, T.B., Wichern, F., Barkholt, P., Vrang, N., Jelsing, J., and Hecksher-Sørensen, J. (2021). An Optimized Mouse Brain Atlas for Automated Mapping and Quantification of Neuronal Activity Using iDISCO+ and Light Sheet Fluorescence Microscopy. Neuroinform *19*, 433–446.

85. Peng, H., Bria, A., Zhou, Z., Iannello, G., and Long, F. (2014). Extensible visualization and analysis for multidimensional images using Vaa3D. Nat. Protoc. *9*, 193–208.

86. Galil, Z. (1986). Efficient algorithms for finding maximum matching in graphs. ACM Comput. Surv. *18*, 23–38.

87. McIntosh, A.R., Bookstein, F.L., Haxby, J.V., and Grady, C.L. (1996). Spatial Pattern Analysis of Functional Brain Images Using Partial Least Squares. Neuroimage *3*, 143–157.

88. Brandes, U. (2001). A faster algorithm for betweenness centrality*. J. Math. Sociol. *25*, 163–177.

89. Brandes, U. (2008). On variants of shortest-path betweenness centrality and their generic computation. Soc. Network. *30*, 136–145.

90. Freeman, L.C. (1977). A Set of Measures of Centrality Based on Betweenness. Sociometry *40*, 35.

91. Humphries, M.D., and Gurney, K.N. (2008). 'Small-World-Ness': A Quantitative Method for Determining Canonical Network Equivalence. PLoS One *3*, e0002051.

STAR★METHODS

KEY RESOURCES TABLE

REAGENT or RESOURCE	SOURCE	IDENTIFIER
Chemicals, peptides, and recombinant proteins		
Phosphate buffer saline tablets	Sigma Aldrich	P4417
Acrilamide	BIO-RAD	1610140
Bisacrilamide	BIO-RAD	1610142
Sodium dodecyl sulfate	Sigma Aldrich	L3771
Boric acid	Sigma Aldrich	B6768
VA044	Wako	011–19365
Triton X-	Sigma Aldrich	X100
2-2′ Thiodiethanol	Sigma Aldrich	166782
4-Hydroxytamoxifen	Sigma Aldrich	H6278
Corn oil	Sigma Aldrich	C8267
Critical commercial assays		
Step through Inhibitory Avoidance	Ugo Basile	40550
Experimental models: Organisms/strains		
Mouse: FosTRAP mice (B6.129(Cg)-Fostm1.1(cre/ERT2)Luo/J × B6.Cg-Gt(ROSA)26Sortm9(CAG-tdTomato)Hze/J)	The Jackson Laboratory	007909
Software and algorithms		
OriginPro	OriginLab	https://www.originlab.com/
ImageJ	Fiji	https://imagej.net/
ZetaStitcher	This manuscript	https://github.com/lens-biophotonics/SPIMlab.
BrainCell Finder	Silvestri et al.[28]	https://github.com/lens-biophotonics/BCFind
Vaa3D	Peng et al.[85]	https://github.com/Vaa3D
ANTs	Avants et al.[33]	https://github.com/ANTsX
Other		
sCMOS Camera for image acquisition	Hamamatsu	Orca Flash 2.0 v4
RAPID autofocus camera	Alkeria	Celera One CO5-S
Galvanometer scanner	Cambridge Technology	6220H
Illumination Objective	Nikon	Plan Fluor EPI 10X NA 0.3
Detection Objective	Olympus	XLPLN10XSVMP
Quartz cuvette	Starna Scientific	3/Q/15/TW
Linear translation stage	Physik Instrumente	M-122.2DD

RESOURCE AVAILABILITY

Lead contact
Further information and requests for reagents may be directed to and will be fulfilled by the lead contact, Dr. Ludovico Silvestri (silvestri@lens.unifi.it).

Materials availability
This study did not generate new unique reagents.

Data and code availability
Normalized densities of TRAPped cells in the different brain regions are publicly available in Supplementary Material (Table S4).

Software and alghoritms used in this paper are publicly available as of the date of publication. links are listed in the key resources table. Any additional information required to reanalyze the data reported in this paper is available from the lead contact upon request.

EXPERIMENTAL MODEL AND SUBJECT DETAILS

All experimental procedures were approved by the Italian Ministry of Health (Authorization n. 512–2018_FC). Alternatives to *in vivo* techniques were not available, but all experiments were conducted according to principles of the 3Rs.

METHOD DETAILS

Animals

Male and female FosTRAP mice (B6.129(Cg)-Fos$^{tm1.1(cre/ERT2)Luo}$/J × B6.Cg-Gt(ROSA)26Sor$^{tm9(CAG-tdTomato)Hze}$/J) were used for this work.[16] They were housed in groups of 3 or 4 with food and water *ad libitum* and were maintained in a room under controlled light and dark cycle (12/12 h; light starts at 7:00 a.m.), temperature (22 ± 2°C), and humidity (55 ± 10%). Adult mice (aged between 3 months and 6 months) were divided in three groups: training (n = 6 males, n = 4 females), test 24h (hours) (n = 5 males, n = 6 females) and test 7d (days) (n = 4 males, n = 4 females).

Behavioral task

All mice were trained and tested using the behavioral paradigm, step-through inhibitory avoidance (IA). Behavioral procedures were performed in a sound-attenuated room, during the light cycle. Mice were manipulated on the three days previous to training session, and were left in the experimental room from the day before the experiment for habituation. Each mouse was subjected to the task separately. The apparatus consists of an automatic controller and a box (47 × 18 × 25 cm, Ugo Basile, Comerio, Italy) which is divided into two separate compartments by a sliding door. The start compartment is brightly-illuminated while the escape one is dark and connected to the shocker. During the training session, every mouse was gently placed in the brightly-illuminated compartment, facing the door and allowing free access to the dark compartment. The apparatus is designed to exploit the natural behavior of mice to move into the dark. For this reason, they rapidly stepped through the door and immediately receive a 0.3 mA mild foot-shock lasting 2 s. Latency was measured using an automated tilting-floor detection mechanism. After the foot-shock, mice were immediately removed from the dark box, and received the 4-OHT injection. The retention test was carried out 24 h or 7 d after the training session. All mice were trained, randomly assigned to be tested 24h or 7d after training. During the test sessions, trained animals were placed again into the light compartment and latency (s) to entered the dark compartment was recorded. The procedure is thus identical to the training session, but mice do not receive shocks. Five minutes is the maximal latency time given for stepping in the dark. At the end of 300 s, mice that do not step through are removed from the apparatus. After removal from the system, all animals received the 4-OHT injection. The latency to step through was considered a direct measurement of memory.

Delivery of 4-OHT

Mice were handled and got used to needle pain with saline solution daily for at least 3 days prior to the 4-OHT injection. 4-OHT (Sigma H6278) was first dissolved in absolute ethanol to give a final concentration of 20 mg/mL. This stock was then mixed with corn oil (Sigma C8267) at 37°C in order to get an emulsion. The injectable oil formulation was obtained using the Eppendorf ThermoMixer C. The emulsion was heated and shaken for 2 h until the ethanol was entirely evaporated. At this time, the drug was totally dissolved in corn oil and kept at 37°C. 4-OHT (50 mg/kg) was delivered by intraperitoneal (i.p.) injection with a 22 gauge needle.

Ex-vivo brain processing

One week after 4-OHT injection, animals were deeply anesthetized with isoflurane (1.5%–2%) and transcardially perfused with 50 mL of ice-cold 0.01 M phosphate buffered saline (PBS) solution (pH 7.6), followed by 75 mL of freshly prepared paraformaldehyde (PFA) 4% (w/v, pH 7.6). Brains were extracted and prepared according to the CLARITY/TDE protocol (Chung et al., 2013; Costantini et al., 2015). Immediately after perfusion, brains were post-fixed in PFA overnight at 4°C. The day after, samples were incubated in a hydrogel solution (containing 10% acrylamide (v/v), 2.5% bis-acrylamide (v/v) and 0.25% VA044 (w/v) in PBS) at 4°C for 3 days, allowing a sufficient diffusion of the solution into the tissue. Samples were then degassed, replacing oxygen inside the vials with nitrogen, and incubated in a water bath at 37°C for 3 h in order to initiate polymerization of the hydrogel. After 3 h, embedded brains were placed in a clearing solution (containing 4.4% (w/v) sodium dodecyl sulfate (SDS) and 1.2% (w/v) boric acid in ultra-pure water, pH 8.5) at 37°C. Clearing solution was changed every 2–3 days. Specimens were gently shaken throughout the whole clearing period, which typically takes 3–4 weeks. When the samples appeared sufficiently transparent, they were incubated 1 day in PBS with 0.1 Triton X-(PBST, pH 7.6) and 1 day in PBS (pH 7.6), removing the excess SDS. Finally, murine brains optically cleared with serial immersions of mixtures containing 20% and 40% 2-2′ Thiodiethanol (TDE) in PBS, each for 1 day while rotating. The last mixture (40% TDE) was used as an index-matching solution for our imaging (Di Giovanna et al., 2019).

Light-sheet microscopy

The custom-made light-sheet microscope, exploiting RAPID autofocusing, has been described in detail in our previous works.[28,31] In brief, the sample is illuminated from the side using a virtual light sheet created with a galvanometer scanner (6220H, Cambridge Technology), coupled via a 4f system to an air objective (Plan Fluor EPI 10X NA 0.3, Nikon) covered with a protective coverslip. Light emitted from the specimen is detected orthogonally to the illumination plane using an immersion objective corrected for clearing solutions (XLPLN10XSVMP 10X NA 0.6, Olympus). Then, it is bandpass-filtered to isolate fluorescence light and projected by a tube lens onto the chip of a scientific complementary metal-oxide-semiconductor (sCMOS) camera (Orca Flash 2.0, Hamamatsu) operating in rolling-shutter mode to guarantee confocal line detection. During imaging, the sample was fixed in a refractive index-matched quartz cuvette (3/Q/15/TW, Starna Scientific) and moved using a set of high-accuracy linear translators (M-122.2DD, Physik Instrumente). Sample-induced defocus is measured in real-time using RAPID,[28] and correction was implemented by moving the objective with an additional linear translation stage (M-122.2DD, Physik Instrumente). Since an entire mouse brain is too thick to be imaged with our objective, which has a working distance of 8 mm, we imaged the two-halves separately, with an overlap thickness of about 1 mm (Figure S6A). The entire system was controlled by custom software written in C++, available at https://github.com/lens-biophotonics/SPIMlab.

Image analysis

Tiled images acquired with LSM were stitched together using ZetaStitcher (https://github.com/lens-biophotonics/ZetaStitcher). As well as generating a low-resolution view of the entire imaging volume (with voxel side 25 μm), this software includes an application programming interface (VirtualFusedVolume) to access the high-resolution volume. Images were then visualized using FIJI/ImageJ (https://fiji.sc). The two different brain halves were spatially registered with an affine transformation using Advanced Normalization Tools (ANTs) on the low-resolution reconstructions (Figure S6B).

Whole-brain cell detection

Fluorescently labeled neurons were localized in the whole-brain images using BrainCell Finder[29] (https://github.com/lens-biophotonics/BCFind). In brief, patches of the original dataset (accessed via VirtualFusedVolume) were fed into a UNet with four contraction layers of 3D convolutions with an exponentially increasing number of filters, and four expansion layers of transposed 3D convolutions with a decreasing number of filters. UNet training was carried out with binary cross-entropy loss and Adam optimizer. The goal of this network is to perform semantic deconvolution, that is, to transform the original image into an ideal one in which cell bodies are clearly visible, while other structures such as dendrites and axons are removed. The network was previously trained on a ground-truth dataset in which a human expert has localized the centers of neuronal somata. The training dataset was composed of 221 image stacks for a total volume of approximately 6.8 mm^3 and 19′166 manually labeled cells. The stacks were randomly selected from different samples and different areas of the brain, to train the network to recognize the large variability in cell shape that can be found across the sample. The images deconvolved by the network are then processed with a standard blob detection algorithm (difference of Gaussians, DoG) to identify the center of bright structures, which in this case are the neurons. The overall performance of the method is evaluated by comparing the list of neuron centers found by the software with the human-annotated ground-truth test set of 57 image stacks for a total volume of approximately 1.8 mm^3 and 1′786 manually labeled cells. Again, these stacks were randomly selected from different samples and different areas of the brain, to test network performance in different contexts. If two neuron centers from the two annotations (automatic and manual) are closer than 10 μm (approximately half of the average diameter of a neuron), they are considered to be the same cell, that is, a true positive (TP). If a center is present only in the manual annotation, it is considered a false negative (FN), whereas if it is present only in the results of the algorithm, it is considered a false positive (FP). The counting of true positives, false positives and false negatives was carried out using the maximum bipartite matching algorithm.[86] We evaluated localization performance using the formulas precision = TP/(TP + FP) and recall = TP/(TP + FN), and the F1-score, which is defined as the harmonic mean of precision and recall. For our test set, the precision was 0.80, the recall was 0.64 and the F1-score was 0.71. All annotations of cell positions were performed using Vaa3D (https://github.com/Vaa3D). Parameters of the U-Net structure and training are summarized in Table S1.

Spatial registration to reference atlas

The downsampled version of the whole-brain dataset was spatially registered to the Allen reference atlas using ANTs,[33] with a sequence of affine and diffeomorphic (that is, symmetric normalization) transformations (Figure S7A). In detail, images first underwent a strong gamma correction (with exponent 0.3) to reduce dynamic range and increase the relative contribution of tissue autofluorescence over labeled cells. Then, affine registration between single brains and reference atlas was computed. To reliably assess non-linear deformations introduced by clearing, 3 gross brain regions (cerebellum, hippocampi and olfactory bulbs) were manually segmented. A diffeomorphic transformation was then computed to match the segmented areas with the corresponding ones in the reference atlas. Since this step is needed only to correct large-scale deformations, it is computed on further downsampled versions of the data (100 μm voxel side). Eventually, fine registration to the atlas was computed using a diffeomorphic transformation between the real image and the reference image. This sequence of transformations (including alignment of back and front brain halves) were applied to the point clouds produced by the BrainCell Finder, to represent the position of activated neurons in the reference space. Each cell was then assigned to a selected brain area based on its position. To evaluate registration accuracy, 10 reference points

were manually marked in 10 different aligned brains and in the reference atlas (Figure S7B). Then, the Euclidean distance between pairs of corresponding points (samples vs. atlas) was calculated for each point and each sample (100 measures in total). The root-mean-square average value of the distance (0.30 ± 0.08 mm, mean ± s.d.) was considered as the alignment error.

QUANTIFICATION AND STATISTICAL ANALYSIS

Behavioral statistical analysis was performed in OriginLab (2022). The comparisons of acquisition and retention latency times are analyzed by two-way ANOVA (variables: sex and experimental class), followed by Bonferroni's post-hoc comparisons tests. The level of significance was set at *$p < 0.05$, **$p < 0.01$ (training n = 6 males and n = 4 females, test 24h n = 5 males and n = 6 females and test 7d n = 4 males and n = 4 females). Data are shown as mean ± SEM of 4–6 animals for each group (Figure 2B).

Partial least square analysis

The effect of each experimental group on regional cell counts were evaluated using Task PLS.[36,87] Briefly, a dummy matrix with as many columns as the number of subjects and as many lines as the experimental classes was prepared, with 1 in the matrix elements corresponding to the right matching subject-class and 0 elsewhere. This was multiplied by the regional count matrix (as many lines as the subjects, as many columns as the brain areas analyzed) normalized by the volume of each area and by the total number of labeled cells per animal, and the product was processed using singular value decomposition. The resulting left and right matrices contained the contrasts and the saliences, respectively. These identify latent variables in the spaces of experimental classes and in the space of cell counts that best explain the variability observed in the data. Statistical error was calculated using the bootstrap technique by resampling 1000 times with replacement. The reported saliences are the raw ones divided by the standard deviation of the bootstrap results, and can thus be interpreted as z-values. In this sense, the dashed lines in Figure 2C represent different significance levels ($p < 0.1$, $p < 0.05$, $p < 0.01$).

Functional network generation

The inter-regional correlation[25] was calculated for each group of mice in order to quantify the co-variation of activated cell counts in 48 brain regions across mice of each group. As fro the PLS, counts normalized by area volume and by total number of labeled cells per animal were used. The functional connections between different regions were identified by imposing a suitable threshold for the inter-regional correlation. A Monte Carlo simulation was performed to estimate the propagation of error in the correlation coefficient arising from uncertainties in the experimental counts. In each simulation iteration, Gaussian noise was introduced to the experimentally measured counts. Specifically, a total of 100 simulations were conducted, wherein a randomly sampled value was added to each count. The random values were sampled from a Gaussian distribution with a mean centered on the experimentally measured value c_i and a variance equal to $0.06 \times c_i$. The standard deviation of the p values was estimated as the standard deviation of the values obtained from the simulations. The threshold was defined to identify cross-correlations with a p value of less than 0.05, which was a conservative estimate for p values smaller than 0.1 considering neuron counting error. Starting from the correlation matrix and the given threshold value, the corresponding adjacency matrix was computed for each group of mice. Each adjacency matrix defines a corresponding network where the nodes are the 48 brain regions and the links are the functional connections between the regions: positive links correspond to excitatory functional connections and negative links to inhibitory functional connections. The degree centrality of the nodes was calculated by counting the number of connections of each node without considering the sign of the connections, and was normalized on the maximum number of potential connections (in this case 47). The betweenness centrality and the small world coefficient σ were calculated by means of the algorithms betweenness_centrality and sigma of the Python package networkx based on[88–90] and,[91] respectively.